

Nanoscale

rsc.li/nanoscale

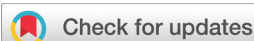


ISSN 2040-3372



PAPER
Jorge Pérez-Juste, Mei Hong *et al.*
Shape control in ZIF-8 nanocrystals and metal nanoparticles@ZIF-8
heterostructures





Cite this: *Nanoscale*, 2017, **9**, 16645

Shape control in ZIF-8 nanocrystals and metal nanoparticles@ZIF-8 heterostructures†

Guangchao Zheng,^{a,b} Zhuwen Chen,^a Kadir Sentosun,^c Ignacio Pérez-Juste,^b Sara Bals,^c Luis M. Liz-Marzán,^{b,d,e} Isabel Pastoriza-Santos,^b Jorge Pérez-Juste^b *^b and Mei Hong^b *^a

Shape control in metal–organic frameworks still remains a challenge. We propose a strategy based on the capping agent modulator method to control the shape of ZIF-8 nanocrystals. This approach requires the use of a surfactant, cetyltrimethylammonium bromide (CTAB), and a second capping agent, tris(hydroxymethyl) aminomethane (TRIS), to obtain ZIF-8 nanocrystals with morphology control in aqueous media. Semiempirical computational simulations suggest that both shape-inducing agents adsorb onto different surface facets of ZIF-8, thereby slowing down their crystal growth rates. While CTAB molecules preferentially adsorb onto the {100} facets, leading to ZIF-8 particles with cubic morphology, TRIS preferentially stabilizes the {111} facets, inducing the formation of octahedral crystals. Interestingly, the presence of both capping agents leads to nanocrystals with irregular shapes and higher index facets, such as hexapods and burr puzzles. Additionally, the combination of ZIF-8 nanocrystals with other materials is expected to impart additional properties due to the hybrid nature of the resulting nanocomposites. In the present case, the presence of CTAB and TRIS molecules as capping agents facilitates the synthesis of metal nanoparticle@ZIF-8 nanocomposites, due to synergistic effects which could be of use in a number of applications such as catalysis, gas sensing and storage.

Received 25th May 2017,
Accepted 24th July 2017

DOI: 10.1039/c7nr03739b

rscl.li/nanoscale

Introduction

Metal–organic frameworks (MOFs) have found wide applications in various fields such as energy, catalysis and drug-delivery.^{1,2} Rational design of the chemical and physical properties of MOFs relies on structural aspects, such as their size and morphology, but also on their composition.^{3–6} Typical synthesis procedures result in bulk MOF powders with relatively large crystal sizes, random shapes, and high polydispersity. However, control over MOF crystal morphology in the nanometer scale is a pre-requisite in certain fields such as optoelectronics or biomedical applications.⁷ Different approaches have been developed to control the size and morphology of MOFs, which typically focus on controlling the kinetics of the

growth process.⁸ The main strategy explored so far toward morphology control has been based on the coordination modulation method, in which different additives are used to modulate crystal growth, by influencing coordination equilibria.^{9,10} For instance, Tsuruoka *et al.* added acetic acid as a competitor to alter the coordination equilibria between copper ions and organic linkers.¹¹ This competitive interaction determined the reaction rate and induced anisotropic crystal growth through oriented attachment. Similarly, Umemura *et al.* have shown an octahedron–cuboctahedron–cube morphological transition in a [Cu₃(btc)₂]_n crystal by tuning the concentration of lauric acid.¹² The presence of the modulator induced MOF crystal growth along the [111] and [100] directions, which eventually dictated the final shape. Alternatively, surfactant molecules have also been reported to act as modulators.¹³ The role of surfactants as capping agents and their adsorption onto specific crystal facets could also induce a morphological evolution. Pan *et al.* demonstrated that the presence of cationic surfactants could change the morphology of ZIF-8 MOFs, from truncated cubic to rhombic dodecahedron.¹⁴ The different adsorption affinities of the surfactant molecules towards the {100} and {110} facets have been invoked as the main factor modulating their relative growth rate.

We recently demonstrated that the surfactant-based approach could also be applied to the synthesis of metal nanoparticle@ZIF-8 heterostructures. The adsorption ability of

^aGuangdong Provincial Key Laboratory of Nano-Micro Materials Research, School of Chemical Biology & Biotechnology, Peking University Shenzhen Graduate School, Shenzhen 518055, China. E-mail: hongmei@pkusz.edu.cn

^bDepartamento de Química Física and CINBIO, Universidade de Vigo, 36310 Vigo, Spain. E-mail: juste@uvigo.es

^cEMAT-University of Antwerp, Groenenborgerlaan 171, B-2020 Antwerp, Belgium

^dBionanoplasmonics Laboratory, CIC biomaGUNE, 20014 Donostia-San Sebastián, Spain

^eIkerbasque, Basque Foundation for Science, 48013 Bilbao, Spain

† Electronic supplementary information (ESI) available: Additional SEM images and EDX characterization, FTIR, N₂ physisorption isotherms, TG analysis and supporting information videos. See DOI: 10.1039/c7nr03739b

quaternary ammonium surfactant molecules towards both metal surfaces and ZIF-8 metal organic frameworks enhanced their interaction and facilitated the formation of nanostructures with core-shell metal nanoparticle-ZIF-8 morphology.¹⁵ We also showed that the same approach could be applied to surfactant stabilized nanoparticles of arbitrary shapes. Here, we target an aqueous-based general approach to modulate the morphology of ZIF-8 nanocrystals that, at the same time, allows us to obtain hybrid core-shell morphologies involving metal nanoparticle cores. Particularly, we implement the capping agent modulation method based on the presence of two modulators, simultaneously, throughout the crystal growth. The addition of cetyltrimethylammonium bromide (CTAB) together with tris(hydroxymethyl)aminomethane (TRIS) leads to a cooperative effect that modulates the final morphology of ZIF-8 nanocrystals from cubic to octahedral, hexapods, burr puzzles and flower-like shapes.

Results and discussion

The presence of CTAB as a capping agent induced the formation of ZIF-8 nanocrystals with poly-cubic morphology,

as previously reported, through the preferential stabilization of the [100] facets (see Fig. 1A). Additionally, careful tuning of the CTAB concentration (below its critical micelle concentration, cmc) in the reaction medium allows us to vary the final particle size.¹⁴ On the other hand, the use of TRIS instead of CTAB led to nanocrystals with different morphologies, which could be modulated *via* TRIS concentration. Whereas the presence of 10 mM TRIS induced the formation of rough octahedral nanocrystals (Fig. 1B), by increasing the concentration to 50 mM and 100 mM flake-shaped and flower-like nanoparticles were obtained, respectively (see Fig. 1C and D). We additionally studied the combined influence of both modulators, CTAB and TRIS, on the morphology of MOF particles. Interestingly, in the presence of 0.07 mM CTAB and 10 mM TRIS, particles with well-defined hexapod morphology were formed (see Fig. 1E), but when the amount of TRIS is increased to 50 mM, the particles displayed multiple arms, in a sort of burr puzzle (see Fig. 1F). It should be noted that if CTAB concentration was increased to 0.35 mM, its modulating effect dominated and particles with cubic morphology were obtained.¹⁴

Different techniques such as electron microscopy, X-Ray diffraction and Fourier transform infrared (FTIR) spectroscopy

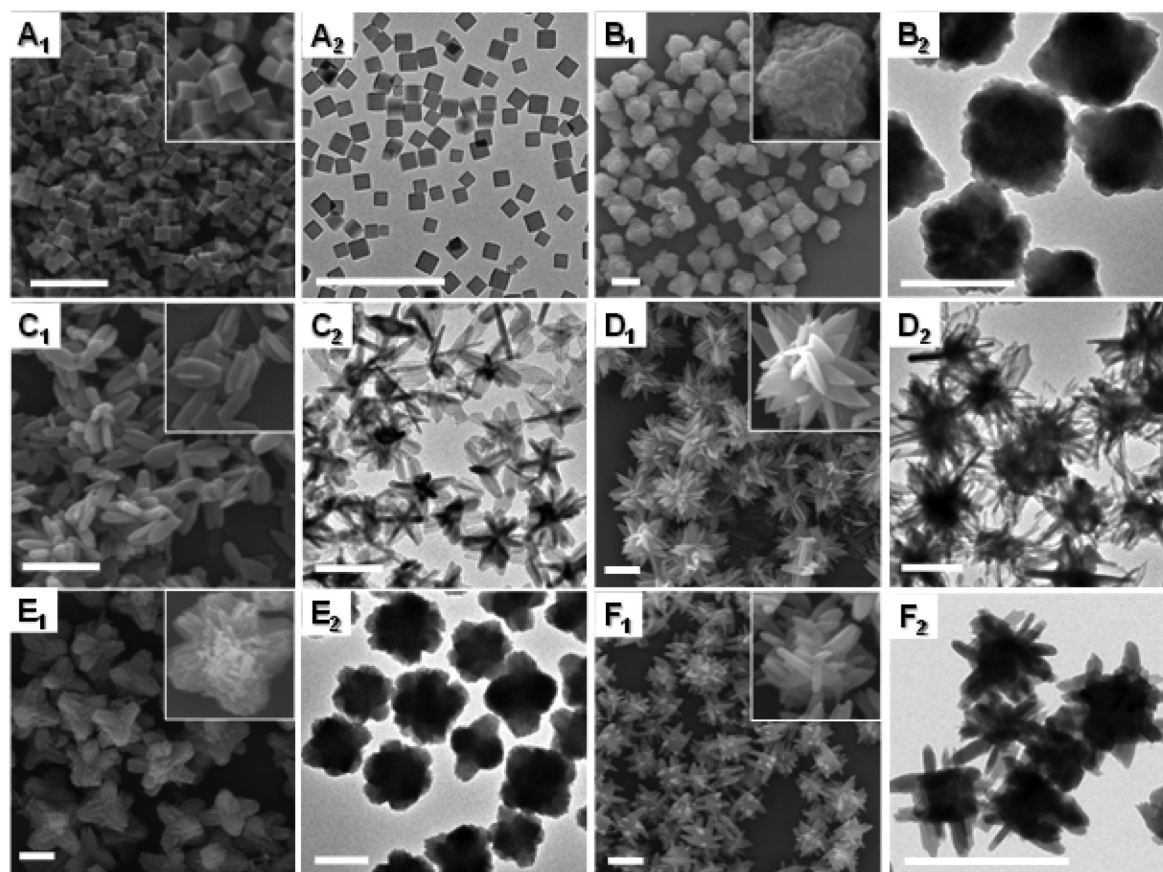


Fig. 1 Representative SEM (1) and TEM (2) images of ZIF-8 nanocrystals synthesized in the presence of different capping agents: (A) 0.07 mM CTAB, (B) 10 mM TRIS, (C) 50 mM TRIS, (D) 100 mM TRIS, (E) 0.07 mM CTAB and 10 mM TRIS, and (F) 0.07 mM CTAB and 50 mM TRIS. The insets in the SEM images show particles at a higher magnification. Scale bars represent 1 μm .

were used to characterize the influence of CTAB and/or TRIS on the final morphology and structure of the particles. Fig. 2A shows the powder XRD patterns, recorded from MOFs synthesized in the presence of different amounts of CTAB and/or TRIS. All diffraction patterns exhibit the characteristic peaks (011), (002), (112), (022), (013) and (222), indexed to the unit cell of the SOD-type ZIF-8 structure, confirming that all the samples were of the pure ZIF-8 phase, with high crystallinity.¹⁶ It should be pointed out that in the case of flake-like nanoparticles (no CTAB; 50 mM TRIS) the XRD pattern reveals the presence of additional peaks at *ca.* 11, 15 and 17 degrees. These peaks can be ascribed to the presence of a ZIF pseudopolymorphism due to the partial deprotonation of 2-methyl-

imidazole.^{17,18} Additionally, selected area electron diffraction (SAED) was performed on ZIF-8 nanocrystals with burr puzzle morphology. Shown in Fig. 2C is the SAED pattern from the single particle displayed in Fig. 2B, along the [111] direction with respect to the electron beam. Additional reflections (one of them highlighted with a green arrow) are also observed, suggesting that the particle is polycrystalline. Elemental distribution in the same nanocrystal was visualized by EDX mapping. Fig. 2D shows the representative SEM images and the corresponding EDX mapping for a burr puzzle particle (see additional SEM and EDX mappings for nanocrystals with cubic, flake and flower-like morphologies in Fig. S1, in the ESI†). In all cases, it can be clearly observed that Zn, N and C are homogeneously distributed throughout the particles. The different ZIF-8 morphologies were also analyzed by FTIR spectroscopy (see Fig. S2†). All spectra show the characteristic bands of ZIF-8, being dominated by the vibration of the imidazole units, without significant differences between different morphologies and in agreement with those reported in the literature.^{19,20} The absence of vibrational bands characteristic of amines and hydroxyl groups, characteristic of TRIS, or CN vibrational modes and CH stretching from CTAB indicates that neither of the shape modulating molecules were retained in the pores of the ZIF-8 nanocrystals and served as capping and shape-inducing agents only.

The surface area of the different ZIF-8 nanocrystals was characterized by nitrogen adsorption isotherms (see Fig. S3 and Table S1 in the ESI†). All samples showed typical type-I adsorption isotherms characteristic of nanoscale ZIF-8 and in overall agreement with reported data for microscale and nanoscale ZIF-8.^{16,21} The increase in the adsorbed nitrogen amount at high relative pressures ($p/p_0 > 0.8$) with a small adsorption-desorption hysteresis loop can be ascribed to the presence of intercrystalline and interparticle mesopores between adjacent nanocrystals.²¹ The BET surface area values estimated for the cubic, octahedron and burr puzzle ZIF-8 nanocrystals are within the range of values previously reported for pure ZIF-8.²² Nevertheless, the surface area of the flake-like nanoparticles is however well below this range ($306.9 \text{ m}^2 \text{ g}^{-1}$), which may be

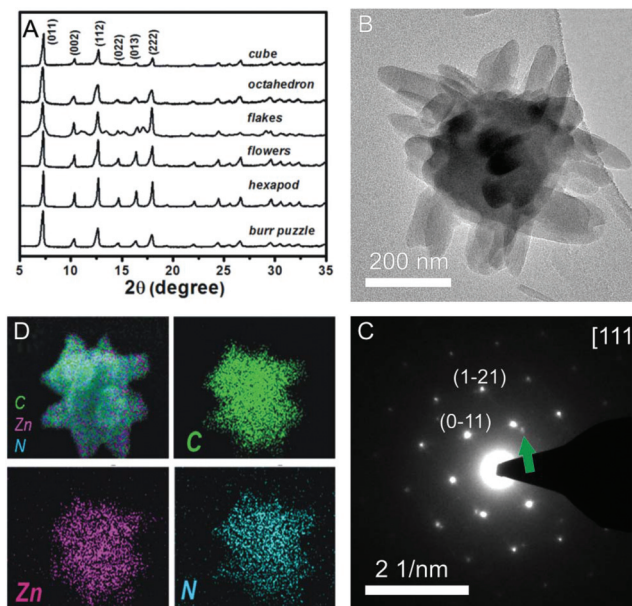


Fig. 2 (A) XRD patterns of different ZIF-8 nanocrystals obtained in the presence of different amounts of CTAB and/or TRIS. (B) Bright field TEM image of a burr puzzle crystal; its corresponding diffraction pattern is shown in (C). (D) EDX elemental mapping of a burr puzzle ZIF-8 nanocrystal.

Table 1 Calculated interaction energies in kcal mol^{-1} , obtained from PM7 semiempirical calculations and schematic representation of the ZIF-8 unit cell, highlighting the {100} and {111} facets (left) and sketches of the most stable interactions with TRIS and CTAB molecules (center and right, respectively)

	{100}	{111}	{-1-1-1}
TRIS	-30.8	-32.1	-37.4
CTAB	-87.0	-84.6	-75.5

related to the presence of ZIF-8 pseudopolymorphism, which has been reported to present almost no porosity.^{17,23} Additionally, the thermogravimetric analysis performed on the samples reveals that the nanocrystals are stable in air up to *ca.* 200 °C before decomposition of the framework structure takes place (see Fig. S4 in the ESI†). The stability of the different ZIF-8 nanocrystals was evaluated with time upon storage in methanol. The results demonstrated that all nanocrystals retain their shape, except the flower-like nanoparticles, which slightly reshape/dissolve with time (see Fig. S5 in the ESI†). The different behavior of the flower-like nanoparticles could be related to the lower yield of the reaction and therefore their thermodynamic stability might be lower (see Table S1 in the ESI†).

According to the Wulff's rule, from a thermodynamic perspective the most stable crystal morphology is dictated by the relative surface energies of the different facets, *i.e.* the slow-growing facet.²⁴ Typically, in the nanometer range, addition of capping agents of distinct nature can result in variations of the growth rate of different facets, leading to nanocrystals with a wide variety of morphologies.^{25,26} In the present case, in the absence of a capping agent, ZIF-8 nanocrystals present a rhombic dodecahedron shape with a mixture of {100} and {110} facets. Oppositely, in the presence of capping agents such as CTAB or TRIS, particles were obtained with cubic or octahedron morphology, respectively. Bearing in mind that neither of the two capping agents were incorporated within the MOF structure, as demonstrated by FTIR characterization, we propose that their interaction with the different crystal facets leads to different crystal growth modes. In order to confirm this hypothesis, we calculated intermolecular interactions between ZIF-8 and TRIS, using a model formed by a unit cage of ZIF-8, comprising 708 atoms, and a TRIS unit, similar to that previously reported for CTAB.¹⁵ The crystallographic unit cell of ZIF-8 is composed of a combination of {111} and {100} facets (see Table 1). A conformational analysis of the TRIS molecule showed that the most stable conformer presents three anti NCCO units. Using the PM7 semiempirical method, we carried out geometrical optimizations for different orientations between the TRIS unit and the three facets of the ZIF-8 unit and computed their interaction energies (see the Experimental section for details). Selected minimized representative conformations and interaction energies are shown in Fig. S4 in the ESI.† The obtained negative values clearly indicate the existence of stabilizing interactions between ZIF-8 and TRIS for different geometries and relative orientations (see Table 1). Although the interaction energies are similar, they indicate that adsorption on the {111} facets is slightly preferred. We thus conclude that the adsorption of CTAB and TRIS on ZIF-8 takes place preferentially on {100} and {111} facets, respectively.

Even though MOFs display unique properties, the incorporation of functional guests or their combination with other materials is expected to impart additional properties due to the hybrid nature of the resulting nanocomposites.^{27–29} In the present case, the presence of CTAB and TRIS molecules as

capping agents largely facilitates the synthesis of metal nanoparticle@ZIF-8 nanocomposites, due to a synergistic effect; on the one hand, both molecules can modulate the morphology of ZIF-8 nanocrystals, and on the other hand the presence of CTAB molecules can promote the nucleation and growth of ZIF-8 nanocrystals on the surface of pre-synthesized plasmonic nanoparticles, giving rise to hybrid nanostructures. We have recently shown that the presence of quaternary

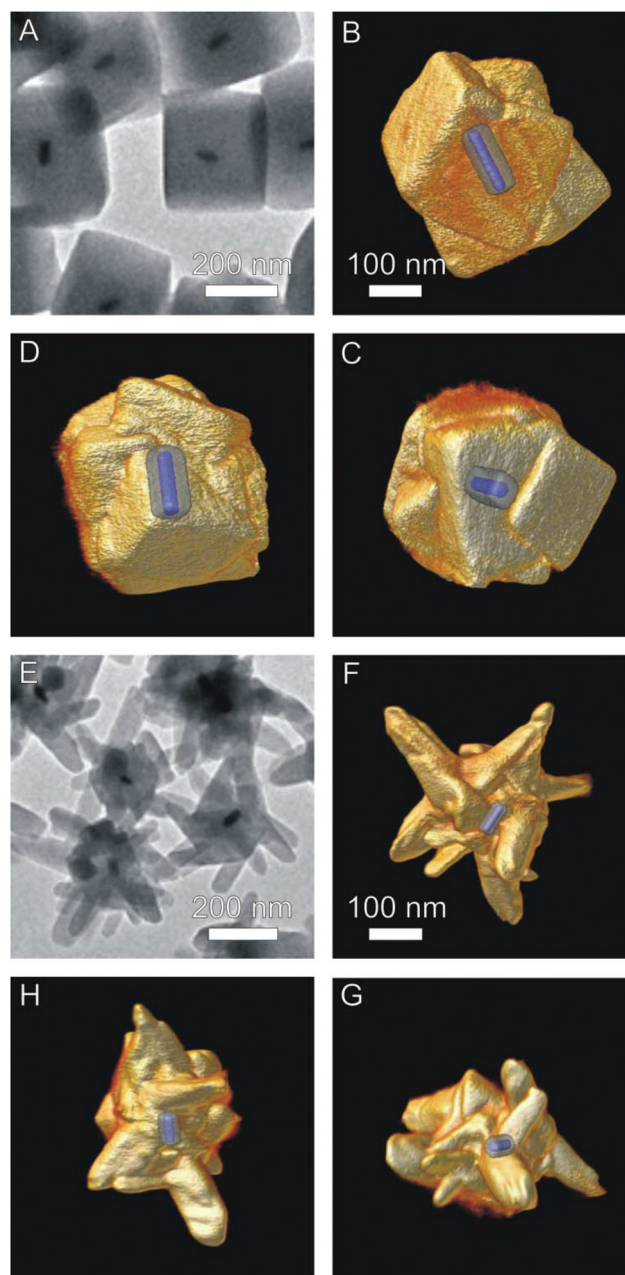


Fig. 3 Representative TEM images of Au@Ag nanorods encapsulated within cubic (A) and burr puzzle (E) ZIF-8 nanocrystals, and visualizations of the corresponding 3D reconstructions, from a cubic (B, C, and D) and a burr puzzle (F, G, and H) ZIF-8 coated nanoparticle, demonstrating core-shell configurations. See ESI Videos SV1 and SV2† for full reconstructions.

ammonium surfactants resulted in the encapsulation of individual plasmonic nanoparticles by ZIF-8 MOFs.¹⁵ The presence of CTAB was shown to lead to a polycrystalline ZIF-8 shell comprising several cubic nanoparticles, likely due to multiple ZIF-8 nucleations on the metal surface. Similarly, the simultaneous presence of CTAB and TRIS molecules should allow us to synthesize core-shell metal NP@ZIF-8 hybrids with shells of different morphologies. Fig. 3 shows the representative TEM images of Au@Ag nanorods encapsulated within the ZIF-8 shells, grown in the presence of only CTAB (0.07 mM, cubic morphology) or a mixture of CTAB (0.07 mM) and TRIS (50 mM). The 3D morphology of the core-shell nanoparticles was characterized by electron tomography. A dedicated procedure was used to image both heavy and light elements in the same sample, in a dose efficient manner.³⁰ Visualizations of the 3D reconstructions are presented in Fig. 3 and the videos are available as ESI (SV1 and SV2†). The MOF shells are highlighted in yellow, whereas Ag and Au in the nanorods are labelled with grey and blue colors, respectively. The 3D reconstructions reveal that Au@Ag NRs are entirely surrounded by the MOF shells, which are indeed formed by several ZIF-8 cubes, oriented along different directions for the particles synthesized using CTAB, or comprise ZIF-8 spikes with different sizes for the particles synthesized in CTAB/TRIS. The thickness of the spikes was measured using orthoslices from the 3D reconstructions, yielding a variation between 25 nm and 60 nm.

Conclusions

In summary, we report an aqueous based synthesis of ZIF-8 nanocrystals with morphology control, based on the capping agent modulation method using CTAB and TRIS molecules, which adsorb onto the different surface facets of ZIF-8, slowing down their crystal growth rates. While CTAB molecules adsorb preferentially to the {100} facets, leading to ZIF-8 with cubic morphology, TRIS molecules stabilize preferentially the {111} facets and give rise to nanocrystals with octahedral morphology. Interestingly, the presence of both capping agents leads to nanocrystals with irregular shapes and higher index facets, such as hexapods and burr puzzles. Additionally, we have shown that this approach can be extended to the single encapsulation of metal nanoparticles within the hierarchical ZIF-8 nanocrystals. This may open the way toward the development of new methods for ZIF-8 nanocrystals with shape control, which will be of use in a number of applications such as catalysis, gas sensing and storage.

Experimental

Materials

Hexadecyltrimethylammonium bromide (CTAB) and hexadecyltrimethylammonium chloride (CTAC) were purchased from Aladdin; HCl was purchased from Adamas;

2-methylimidazole (HMIM), zinc nitrate hexahydrate ($\text{Zn}(\text{NO}_3)_2 \cdot 6\text{H}_2\text{O}$), gold(III) chloride hydrate, tris(hydroxymethyl) aminomethane (TRIS), silver nitrate and NaCl were purchased from Sigma-Aldrich.

Synthesis of ZIF-8 nanocrystals

The synthetic procedure was based on a previously reported protocol with slight modifications. First, stock solutions of $\text{Zn}(\text{NO}_3)_2 \cdot 6\text{H}_2\text{O}$ (24 mM) and 2-methylimidazole (1.32 M) were prepared in different concentrations of TRIS (0 mM, 10 mM, 50 mM and 100 mM, pH 7.2). Subsequently, 0.145 mL of an aqueous solution of CTAB (1 mM) was added to 1 mL of HMIM stock solution and stirred for 5 min. Then, 1 mL of $\text{Zn}(\text{NO}_3)_2 \cdot 6\text{H}_2\text{O}$ stock solution was added, stirred for 5 min and left undisturbed at room temperature for 3 hours. The final pH is a critical factor toward the successful synthesis of the different ZIF-8 nanocrystals in water since basic pH values lead to the deprotonation of HMIM, thereby promoting the formation of the ZIF-8 structures. In all cases, the final pH in the reaction medium was between 8 and 9, since a pH value below the pK_a 's of HMIM (7.0 and 7.2) leads to its protonation, hindering the nucleation of ZIF-8 nanocrystals. The ZIF-8 nanocrystals were collected by centrifugation and washed several times in methanol and redispersed in ethanol. See Table S1† for a detailed description of the different mixtures analyzed.

Synthesis of metal NPs@ZIF-8 core-shell hybrid nanocrystals

Au nanorods and Au@Ag nanorods are prepared based on previous work.¹⁵ The encapsulation of metal nanoparticles within ZIF-8 was carried out as follows: 1 mL of Au nanorods or Au@Ag nanorods (typically 10 nM) and 145 μL of 1 mM CTAB were injected into 1 mL of 1.32 M HMIM in 50 mM TRIS (pH 7.2) and stirred for 5 min. Thereafter, 1 mL solution containing 24 mM $\text{Zn}(\text{NO}_3)_2$ in 50 mM TRIS (pH 7.4) was added. The resulting mixture was stirred for 5 minutes and left undisturbed for 3 hours. The core-shell Au@Ag@ZIF-8 particles were centrifuged at 5000 rpm for 5 min, washed with 10 mL of methanol and finally redispersed in 5 mL of methanol.

Characterization

UV-visible characterization was performed using a UV-2600 Shimadzu spectrophotometer. Fourier Transform infrared spectroscopy (FTIR) spectra were recorded in KBr pellets on a Shimadzu IR-Prestige 21 spectrophotometer. Conventional TEM images were acquired with a Tecnai G2 microscope operated at 120 kV. Scanning electron microscopy (SEM) was performed on a JEOL JSM-7800F electron microscope operated at 5.0 kV without coating the samples.

Acquisition of the tilt series for electron tomography was performed using a Fischione 2020 single tilt holder and an FEI Osiris electron microscope, operating at an accelerating voltage of 120 kV. The projection images were collected over an angular range between -74° and $+73^\circ$, with a 3° tilt increment. The tilt series was aligned using the FEI INSPECT 3D software and reconstructed *via* the simultaneously iterative reconstruction technique implemented in the ASTRA tomography

toolbox.³⁰ During the acquisition of the projection images, ADF and HAADF detectors were simultaneously used to retrieve information from both low and high atomic number elements. More information about the complete acquisition and the reconstruction procedure can be found in ref. 31.

Powder X-ray diffraction (XRD) patterns of ZIF-8 were recorded using a Bruker D8 Advance PC diffractometer in the diffraction angle range $2\theta = 4\text{--}50^\circ$ with Cu K α radiation ($\lambda = 1.5418 \text{ \AA}$) at 40 kV, 40 mA.

Nitrogen adsorption-desorption isotherms were measured at 77.35 K on a Micromeritics Tristar II 3020 v1.03 analyzer. The powder samples were degassed at 120 °C for at least 12 h prior to the measurements. The Brunauer-Emmett-Teller (BET) surface areas were calculated from the adsorption data from $0.05 < P/P_0 < 0.30$.

Thermogravimetric analysis (TGA) was carried out on a Shimadzu-TGA-50. The sample was maintained at room temperature under a 20 mL min⁻¹ nitrogen flow rate atmosphere, and then heated at a rate of 20 °C min⁻¹ over a temperature range from 25 °C to 600 °C.

Computational methods

The intermolecular interactions between ZIF-8 and the surfactant were studied using semiempirical PM6 and PM7 methods included in MOPAC2012.³² A unit model of ZIF-8 containing 708 atoms was defined and a large number of geometrical optimizations for different orientations between ZIF-8 and either a CTAB surfactant monomer or a TRIS molecule were performed. The interaction energies (E_{int}) for the stable complexes found have been computed as the energy difference $E_{\text{interaction}} = E_{\text{complex}} - (E_{\text{ZIF8}} + E_{\text{TRIS/CTAC}})$, where E_{complex} , E_{ZIF8} , and $E_{\text{TRIS/CTAB}}$ were the computed PM7 energies for the complex, the isolated ZIF-8, and the isolated CTAB or TRIS, respectively, at the optimized geometries of the complex.

Acknowledgements

This work was supported by the Ministerio de Economía y Competitividad (MINECO, Spain), under the Grants MAT2013-45168-R and MAT2016-77809-R. This study was also funded by the Xunta de Galicia/FEDER (ED431C 2016-048). We are grateful to the financial support from the National Natural Science Foundation of China (21671010), the Guangdong Science and Technology Program (2013A061401002), and the Shenzhen Strategic Emerging Industries (KQCX2015032709315529 and CXZZ20140419131807788).

Notes and references

- R. D. Mukhopadhyay, V. K. Praveen, A. Hazra, T. K. Majic and A. Ajayaghosh, *Chem. Sci.*, 2015, **6**, 6583–6591.
- P. Falcaro, R. Ricco, A. Yazdi, I. Imaz, S. Furukawa, D. MasPOCH, R. Ameloot, J. D. Evans and C. J. Doonan, *Coord. Chem. Rev.*, 2016, **307**, 237–254.
- H. S. Cho, H. X. Deng, K. Miyasaka, Z. Y. Dong, M. Cho, A. V. Neimark, J. K. Kang, O. M. Yaghi and O. Terasaki, *Nature*, 2015, **527**, 503–507.
- J. A. Mason, J. Oktawiec, M. K. Taylor, M. R. Hudson, J. Rodriguez, J. E. Bachman, M. I. Gonzalez, A. Cervellino, A. Guagliardi, C. M. Brown, P. L. Llewellyn, N. Masciocchi and J. R. Long, *Nature*, 2015, **527**, 357–361.
- L. Y. Chou, P. Hu, J. Zhuang, J. V. Morabito, K. C. Ng, Y. C. Kao, S. C. Wang, F. K. Shieh, C. H. Kuo and C. K. Tsung, *Nanoscale*, 2015, **7**, 19408–19412.
- L. C. He, M. Brasino, C. C. Mao, S. Cho, W. Park, A. P. Goodwin and J. N. Cha, *Small*, 2017, **13**, 1700504.
- M. Sindoro, N. Yanai, A. Y. Jee and S. Granick, *Acc. Chem. Res.*, 2014, **47**, 459–469.
- C. V. McGuire and R. S. Forgan, *Chem. Commun.*, 2015, **51**, 5199–5217.
- J. F. Yao, M. He and H. T. Wang, *CrystEngComm*, 2015, **17**, 4970–4976.
- B. Seoane, S. Castellanos, A. Dikhtiarenko, F. Kapteijn and J. Gascon, *Coord. Chem. Rev.*, 2016, **307**, 147–187.
- T. Tsuruoka, S. Furukawa, Y. Takashima, K. Yoshida, S. Isoda and S. Kitagawa, *Angew. Chem., Int. Ed.*, 2009, **48**, 4739–4743.
- A. Umemura, S. Diring, S. Furukawa, H. Uehara, T. Tsuruoka and S. Kitagawa, *J. Am. Chem. Soc.*, 2011, **133**, 15506–15513.
- W. W. Xiong and Q. C. Zhang, *Angew. Chem., Int. Ed.*, 2015, **54**, 11616–11623.
- Y. C. Pan, D. Heryadi, F. Zhou, L. Zhao, G. Lestari, H. B. Su and Z. P. Lai, *CrystEngComm*, 2011, **13**, 6937–6940.
- G. C. Zheng, S. de Marchi, V. López-Puente, K. Sentosun, L. Polavarapu, I. Pérez-Juste, E. H. Hill, S. Bals, L. M. Liz-Marzán, I. Pastoriza-Santos and J. Pérez-Juste, *Small*, 2016, **12**, 3935–3943.
- K. S. Park, Z. Ni, A. P. Cote, J. Y. Choi, R. D. Huang, F. J. Uribe-Romo, H. K. Chae, M. O’Keeffe and O. M. Yaghi, *Proc. Natl. Acad. Sci. U. S. A.*, 2006, **103**, 10186–10191.
- W. C. Lee, H. T. Chien, Y. Lo, H. C. Chiu, T. P. Wang and D. Y. Kang, *ACS Appl. Mater. Interfaces*, 2015, **7**, 18353–18361.
- N. A. H. M. Nordin, A. F. Ismail, A. Mustafa, P. S. Goh, D. Rana and T. Matsuura, *RSC Adv.*, 2014, **4**, 33292–33300.
- Y. Hu, H. Kazemian, S. Rohani, Y. N. Huang and Y. Song, *Chem. Commun.*, 2011, **47**, 12694–12696.
- Y. S. Wang, Y. P. Xu, H. J. Ma, R. S. Xu, H. Liu, D. W. Li and Z. J. Tian, *Microporous Mesoporous Mater.*, 2014, **195**, 50–59.
- J. Cravillon, S. Munzer, S. J. Lohmeier, A. Feldhoff, K. Huber and M. Wiebcke, *Chem. Mater.*, 2009, **21**, 1410–1412.
- W. N. Zhang, Y. Y. Liu, G. Lu, Y. Wang, S. Z. Li, C. L. Cui, J. Wu, Z. L. Xu, D. B. Tian, W. Huang, J. S. DuCheneu, W. D. Wei, H. Y. Chen, Y. H. Yang and F. W. Huo, *Adv. Mater.*, 2015, **27**, 2923–2929.
- Z. X. Low, J. F. Yao, Q. Liu, M. He, Z. Y. Wang, A. K. Suresh, J. Bellare and H. T. Wang, *Cryst. Growth Des.*, 2014, **14**, 6589–6598.

- 24 R. Li, X. Zhang, H. Dong, Q. Li, Z. Shuai and W. Hu, *Adv. Mater.*, 2016, **28**, 1697–1702.
- 25 M. Grzelczak, J. Pérez-Juste, P. Mulvaney and L. M. Liz-Marzán, *Chem. Soc. Rev.*, 2008, **37**, 1783–1791.
- 26 E. Ringe, R. P. Van Duyne and L. D. Marks, *J. Phys. Chem. C*, 2013, **117**, 15859–15870.
- 27 L. C. He, Y. Liu, J. Z. Liu, Y. S. Xiong, J. Z. Zheng, Y. L. Liu and Z. Y. Tang, *Angew. Chem., Int. Ed.*, 2013, **52**, 3741–3745.
- 28 L. Y. Chen, Y. Peng, H. Wang, Z. Z. Gua and C. Y. Duana, *Chem. Commun.*, 2014, **50**, 8651–8654.
- 29 X. Liu, L. C. He, J. Z. Zheng, J. Guo, F. Bi, X. Ma, K. Zhao, Y. L. Liu, R. Song and Z. Y. Tang, *Adv. Mater.*, 2015, **27**, 3273–3277.
- 30 K. Sentosun, M. N. S. Ortiz, K. J. Batenburg, L. M. Liz-Marzán and S. Bals, *Part. Part. Syst. Charact.*, 2015, **32**, 1063–1067.
- 31 W. van Aarle, W. J. Palenstijn, J. De Beenhouwer, T. Altantzis, S. Bals, K. J. Batenburg and J. Sijbers, *Ultramicroscopy*, 2015, **157**, 35–47.
- 32 J. J. P. Stewart, *MOPAC2012*, Stewart Computational Chemistry, Colorado Springs, CO, USA.